LETTER

doi:10.1038/nature23878

Impact of a global temperature rise of 1.5 degrees Celsius on Asia's glaciers

P. D. A. Kraaijenbrink[1], M. F. P. Bierkens[1,2], A. F. Lutz[3] & W. W. Immerzeel[1,4]

Glaciers in the high mountains of Asia (HMA) make a substantial contribution to the water supply of millions of people[1,2], and they are retreating and losing mass as a result of anthropogenic climate change[3] at similar rates to those seen elsewhere[4,5]. In the Paris Agreement of 2015, 195 nations agreed on the aspiration to limit the level of global temperature rise to 1.5 degrees Celsius (°C) above pre-industrial levels. However, it is not known what an increase of 1.5 °C would mean for the glaciers in HMA. Here we show that a global temperature rise of 1.5 °C will lead to a warming of 2.1 ± 0.1 °C in HMA, and that 64 ± 7 per cent of the present-day ice mass stored in the HMA glaciers will remain by the end of the century. The 1.5 °C goal is extremely ambitious and is projected by only a small number of climate models of the conservative IPCC's Representative Concentration Pathway (RCP)2.6 ensemble. Projections for RCP4.5, RCP6.0 and RCP8.5 reveal that much of the glacier ice is likely to disappear, with projected mass losses of 49 ± 7 per cent, 51 ± 6 per cent and 64 ± 5 per cent, respectively, by the end of the century; these projections have potentially serious consequences for regional water management and mountain communities.

Temperatures are rising faster in high-altitude regions, including HMA, than in low-lying plains[6]. Possible explanations for this elevation-dependent warming in mountains include the effects of snow albedo and surface-based feedback, water vapour changes and latent heat release, radiative flux changes, surface heat loss and temperature change, and aerosols. A global ensemble of 110 general circulation model (GCM) runs spanning the full range of radiative forcing defined in the Coupled Model Intercomparison Project Phase 5 (CMIP5)[7] (RCP2.6 ($n = 25$), RCP4.5 ($n = 35$), RCP6.0 ($n = 18$) and RCP8.5 ($n = 32$); Supplementary Table 5) shows an evident relation between radiative forcing and projected temperature increase from pre-industrial conditions (1851–1880) to the end of this century (2071–2100, EOC) (Fig. 1). It also shows that the glacierized areas of HMA are consistently warming at much higher rates than the global average and that the difference between global and HMA temperature rises is increasing with radiative forcing (Fig. 1). Compared to the global warming of land masses only, the enhanced warming in HMA is less pronounced, but still evident. From the GCM ensemble, we have selected models that result in a 1.5 °C temperature rise globally relative to pre-industrial conditions ($n = 6$, see Methods). All of the selected models originate from the conservative RCP2.6 model ensemble. The 1.5 °C global increase implies a warming of 2.1 ± 0.1 °C for the glacierized areas in HMA (Fig. 2). Although there is considerable regional variation, with the Hindu Kush warming the most (2.3 °C) and the Eastern Himalaya the least (1.9 °C), all regions warm by more than 1.5 °C. These spatial patterns persist for the RCP2.6, RCP4.5, RCP6.0 and RCP8.5 scenarios, for which considerably higher warming is projected in western parts of HMA (Supplementary Fig. 10). A strong divergence is observed towards the EOC between the 1.5 °C scenario and RCP4.5 (3.5 ± 0.2 °C), RCP6.0 (4.1 ± 0.2 °C), and RCP8.5 (6.0 ± 0.3 °C) (Supplementary Fig. 8).

The Randolph Glacier Inventory (RGI) version 5.0[8] identifies 95,537 glaciers with a total glacier area of 97,605 km^2 in the RGI regions covering HMA (Fig. 2, Supplementary Table 1). Considerable parts of these glaciers, in particular the low-lying glacier tongues, are covered by thick debris mantles caused by erosion from the generally steep headwalls and the subglacial material on which the glaciers reside. The debris is an important control on glacier ablation, and thus on its climate sensitivity. A thin layer of debris accelerates melt because it has a lower albedo than debris-free ice, whereas a debris layer thicker than a few centimetres suppresses melt because it insulates the underlying ice[9–14]. Except for a few small-scale studies[15,16], the role of debris has generally not been taken into account in climate change impact studies over larger regions, mostly because a debris classification of HMA glaciers is not available. Here we develop such a classification using Landsat 8 imagery. For all glaciers larger than 0.4 km^2 (33,587, 91% of the total glacier area, 99.6% of the glacier ice volume), we identify the debris cover by selecting pixels below a normalized difference snow index (NDSI) value and a slope threshold (see Methods). Our results show that about 11% of the glacier area in HMA is covered with debris (Fig. 3), with the largest relative debris-cover in the Hindu Kush (19% of the regional glacier area). We subsequently compute the ice volume stored in each glacier using the GlabTop2 model[17,18], which we convert to mass using a 900 kg m^{-3} ice density[18,19]. We estimate that the total HMA ice mass, excluding glaciers smaller than 0.4 km^2, is 4,754 ± 350 Gt (Fig. 3), with more than one-third of this volume stored in Karakoram glaciers. The relative ice mass under debris in the HMA is 18%, which is considerably larger than the relative ice area under debris. This is caused by the predominance of debris on gently sloping tongues with thick ice. If only the ablation area below the equilibrium

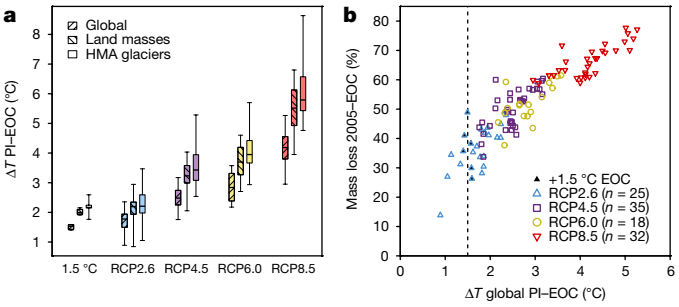

Figure 1 | Relation between radiative forcing, temperature increase and ice mass loss. a, Temperature changes between pre-industrial (PI, 1851–1880) and the end of century (EOC, 2071–2100) for the 1.5 °C models ($n = 6$), RCP2.6 ($n = 25$), RCP4.5 ($n = 35$), RCP6.0 ($n = 18$) and RCP8.5 ($n = 32$). Temperature changes are shown separately for the entire globe, global land mass, and the glaciers of HMA. The horizontal bars denote the median, the boxes the interquartile range, and the whiskers the full data range. **b**, Projected ice mass loss against global temperature change for the EOC for each of the 110 model runs.

[1]Utrecht University, Department of Physical Geography, PO Box 80115, 3508 TC, Utrecht, The Netherlands. [2]Deltares, Daltonlaan 600, 3584 BK, Utrecht, The Netherlands. [3]FutureWater, Costerweg 1V, 6702 AA, Wageningen, The Netherlands. [4]International Centre for Integrated Mountain Development (ICIMOD), GPO Box 3226, Kathmandu, Nepal.

© 2017 Macmillan Publishers Limited, part of Springer Nature. All rights reserved.

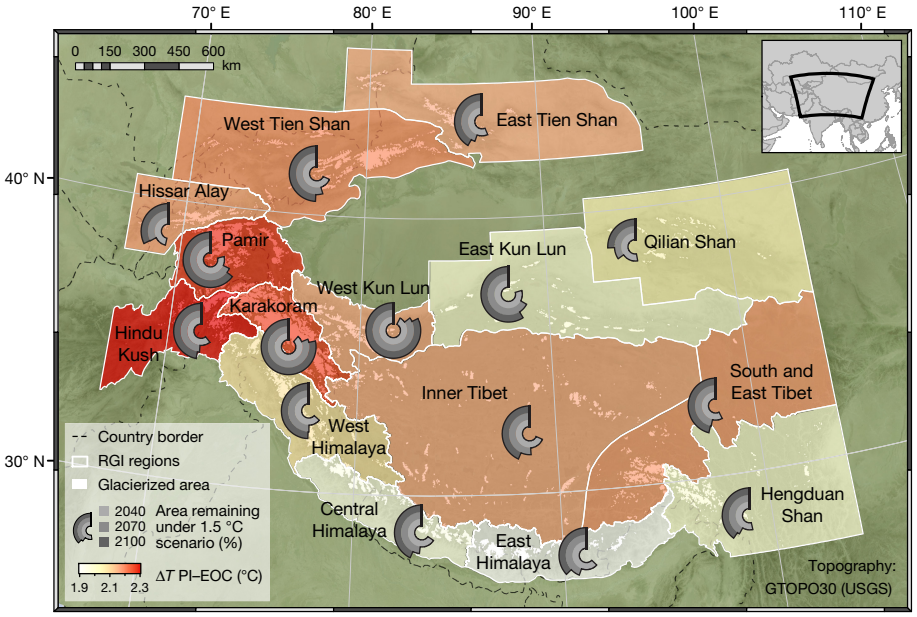

Figure 2 | Regional temperatures and projected glacier area associated with a 1.5 °C increase. The map shows the mean temperature increase at the glaciers between pre-industrial (PI, 1851–1880) and end of century (EOC, 2071–2100) for the global 1.5 °C increase scenario, aggregated by RGI sub-regions[8] (Supplementary Table 1). The circular graphs depict the projected reduction in glacierized area within each region for the 1.5 °C scenario for three points in time.

line altitude (ELA) is considered, the ice mass contribution under debris reaches values of up to 30% in the entire region and up to 48% in the Hindu Kush.

To estimate the response of the HMA glaciers to a global temperature increase of 1.5 °C, we set up a model based on the mass balance gradient[20] for all individual glaciers larger than 0.4 km^2. The mass balance gradient for each glacier is constrained by a maximum ablation at the glacier terminus estimated using degree–day climatology and by a maximum accumulation estimated from the maximum precipitation in the glacier accumulation zone (see Methods). The approach takes into account the reduced melt under debris as function of debris thickness, the increased melt that is due to supraglacial ponds, and the observed regional mass balance[5,21,22] (Supplementary Table 3). Our results indicate that the glaciers are out of balance in all RGI subregions and, except for West Kun Lun, are losing mass under present day (1996–2015) climate conditions (Supplementary Table 3). The results also show that, even if temperatures stabilize at their current level, mass loss will continue for decades to come until a new equilibrium is reached (Fig. 3). For the whole of HMA, about 86% of the present ice mass and 85% of the present-day area would remain by the EOC. To estimate future mass balance, we shifted the present mass balance curve, with a fixed gradient, using the sensitivity of the ELA to temperature change[23] and the projected temperature rise between the present-day climate and the EOC for each of the 110 GCMs (Supplementary Table 5). In addition, we modified the mass balance curve's height of maximum accumulation using projected precipitation change from the same 110 GCMs. To account for the uncertainty in model parameters, observed mass balance and climate projections, the analyses were performed in a Monte Carlo simulation framework, with randomly varying parameter values and mass balance for each GCM forcing for each of the 33,587 glaciers (see Methods). Subsequent results are thus given as the mean ± s.d. from the Monte Carlo runs. The results reveal that if the 1.5 °C target is met, an estimated 64 ± 7% of the ice mass and 64 ± 8% of the glacier area in HMA will remain by the EOC (Figs 1, 3 and Supplementary Fig. 12). In the most extreme case (RCP8.5), the ensemble shows that only 36 ± 5% of the ice mass and 32 ± 5% of the total area will remain by the EOC. RCP2.6 (64 ± 8%), RCP4.5 (51 ± 7%) and RCP6.0 (49 ± 6%) result in intermediate mass losses that fall between the 1.5 °C scenario and RCP8.5. We observe a near-linear relation between temperature increase and projected mass loss at the regional scale (Fig. 1). Only six models out of the entire model ensemble result in a global 1.5 °C increase by the EOC, and the majority of projections result in much greater warming and a larger decrease in HMA ice mass (Fig. 1).

The regional variation in mass loss is large, and there are several regions where for RCP8.5 the ice mass and glacier area drop below 10% of their present-day value (Fig. 3). This will evidently impact the timing of downstream water supply and water access of mountain communities near the glaciers. In particular for RCP8.5 a strong increase in downstream meltwater availability will prevail in the short to medium term with a peak around 2050 (Supplementary Fig. 13), which agrees well with previous findings[15,24]. Meltwater peaks for the remaining RCPs generally occur earlier at around 2030, although for many of the regions peak meltwater has already occurred by this point.

Even under a global 1.5 °C increase, there are considerable regional differences in glacier response within HMA that are caused by differences in regionally projected warming rates and precipitation trends, by specific regional glacier properties (for example, glacier hypsometry and the presence of debris), and by the present-day imbalance of the glaciers (Supplementary Table 3). For example, Hissar Alay and the Qilian Shan are the regions that show the most extreme decline, with only 32 ± 14% and 30 ± 5%, respectively, of the glacier mass remaining by the EOC (Fig. 3). On the other hand, in the Karakoram, despite a higher regional warming rate, 80 ± 7% of the ice mass remains by the EOC. These differences are explained by the large ice masses stored in the debris-covered tongues in the Karakoram compared to Qilian Shan in particular (Fig. 3), by the fact that Qilian Shan and Hissar Alay at present have much more negative mass balances (−0.49 ± 0.11 and −0.36 ± 0.31 metres water equivalent per year, respectively) than the Karakoram (−0.13 ± 0.34 metres water equivalent per year), and by differences in the sensitivity of the ELA to climate perturbations.

Debris on glacier ice plays an important role in regulating melt processes of HMA glaciers[25,26]. It buffers the impact of climate change as the lower melt rates slow down glacier retreat and mass loss under rising temperatures. There is, however, great variability in the relative area covered by debris (Supplementary Fig. 14a), the relative ice mass stored under debris (Supplementary Fig. 14b) and the relative ice mass in the ablation zone stored under debris (Supplementary Fig. 14c).

© 2017 Macmillan Publishers Limited, part of Springer Nature. All rights reserved.

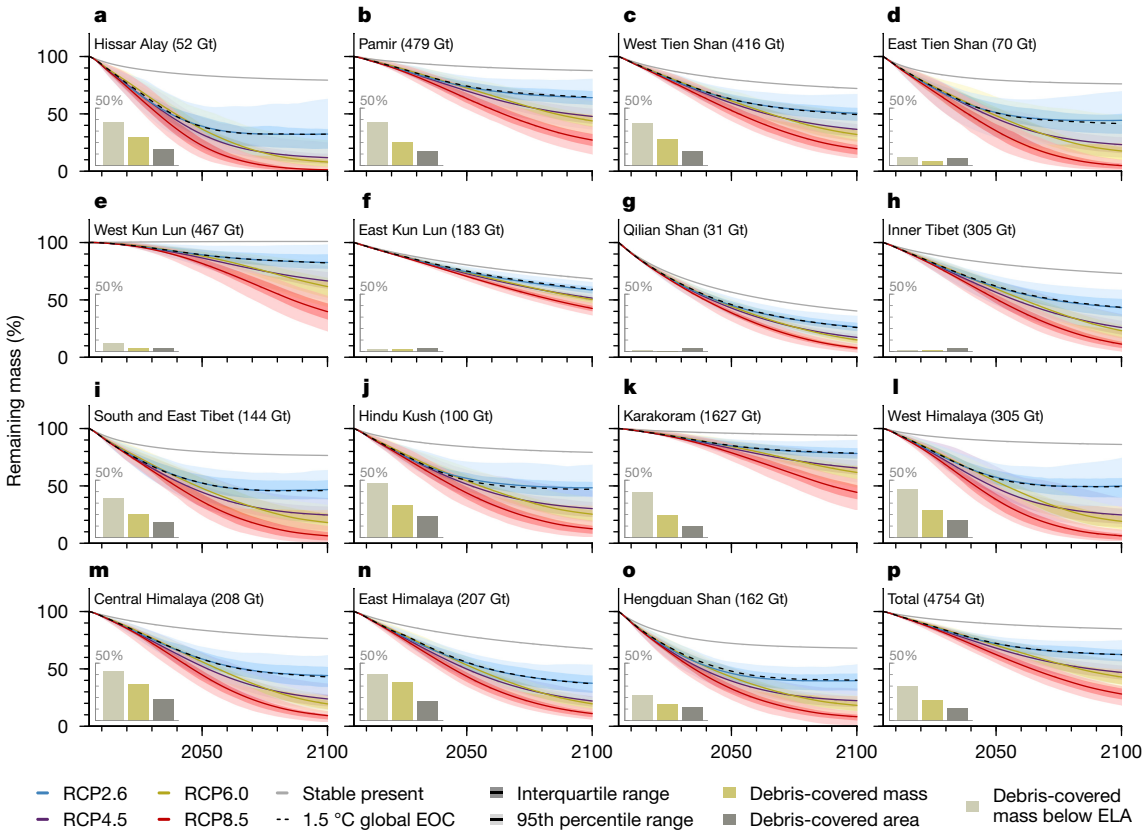

Figure 3 | Future ice mass loss and prevalence of debris-covered glaciers. Mass loss projections aggregated by RGI sub-region (**a**–**o**) and the entire HMA (**p**) for the RCP scenarios, a stable present-day climate, and six models that have a temperature rise of 1.5 °C at the end of century. Error bands are shown for the RCP scenarios, based on the interquartile and 95th percentile range of the Monte Carlo ensemble for each RCP. This includes both the variability between climate models and glacier model parameter uncertainty. The bar charts show the relative presence of debris in each region.

Although the debris-covered area is relatively small, there are regions in the Karakoram and Himalaya where the ice mass under debris in the ablation zones exceeds 40% and this results in a strong buffering effect (Supplementary Fig. 14d–f). As glacier thinning and a rise in the ELA can result in thickening of debris and an increase in debris extent[27], the effects of debris on glacier melt may even increase over the course of the century.

To conclude, HMA is consistently warming more rapidly than the global average. The differences in impact on the glaciers of HMA between the ambitious 1.5 °C target and the RCP4.5, RCP6.0 and RCP8.5 scenarios are large, and may well represent the difference between sustaining the glaciers for generations to come and losing the majority of Asia's glacier ice mass by the EOC. The presence of debris may in some regions provide considerable retention of glacier mass, but clearly policy decisions can make a difference and for the survival of the HMA glaciers it is essential to minimize the global temperature increase. To meet the 1.5 °C target will be a task of unprecedented difficulty and even then, 36 ± 7% of the ice mass in HMA is projected to be lost by the EOC.

Online Content Methods, along with any additional Extended Data display items and Source Data, are available in the online version of the paper; references unique to these sections appear only in the online paper.

Received 20 January; accepted 27 July 2017.

1. Immerzeel, W. W., Van Beek, L. P. H. & Bierkens, M. F. P. Climate change will affect the Asian water towers. *Science* **328,** 1382–1385 (2010).
2. Lutz, A. F., Immerzeel, W. W., Shrestha, A. B. & Bierkens, M. F. P. Consistent increase in High Asia's runoff due to increasing glacier melt and precipitation. *Nat. Clim. Chang.* **4,** 587–592 (2014).
3. Marzeion, B., Cogley, J. G., Richter, K. & Parkes, D. Attribution of global glacier mass loss to anthropogenic and natural causes. *Science* **345,** 919–921 (2014).
4. Bolch, T. *et al.* The state and fate of Himalayan Glaciers. *Science* **336,** 310–314 (2012).
5. Kääb, A., Treichler, D., Nuth, C. & Berthier, E. Contending estimates of 2003–2008 glacier mass balance over the Pamir-Karakoram-Himalaya. *Cryosphere* **9,** 557–564 (2015).
6. Pepin, N. *et al.* Elevation-dependent warming in mountain regions of the world. *Nat. Clim. Chang.* **5,** 424–430 (2015).
7. Taylor, K. E., Stouffer, R. J. & Meehl, G. A. An overview of CMIP5 and the experiment design. *Bull. Am. Meteorol. Soc.* **93,** 485–498 (2012).
8. Pfeffer, W. T. *et al.* The Randolph Glacier Inventory: a globally complete inventory of glaciers. *J. Glaciol.* **60,** 537–552 (2014).
9. Evatt, G. W. *et al.* Glacial melt under a porous debris layer. *J. Glaciol.* **61,** 825–836 (2015).
10. Lejeune, Y., Bertrand, J., Wagnon, P. & Morin, S. A physically based model of the year-round surface energy and mass balance of debris-covered glaciers. *J. Glaciol.* **59,** 327–344 (2013).
11. Vincent, C. *et al.* Reduced melt on debris-covered glaciers: investigations from Changri Nup Glacier, Nepal. *Cryosphere* **10,** 1845–1858 (2016).
12. Reid, T. D., Carenzo, M., Pellicciotti, F. & Brock, B. W. Including debris cover effects in a distributed model of glacier ablation. *J. Geophys. Res.* **117,** D18105 (2012).
13. Pellicciotti, F., Stephan, C., Miles, E., Immerzeel, W. W. & Bolch, T. Mass balance changes of the debris-covered glaciers in the Langtang Himal in Nepal between 1974 and 1999. *J. Glaciol.* **61,** 373–386 (2015).
14. Östrem, G. Ice melting under a thin layer of moraine, and the existence of ice cores in moraine ridges. *Geogr. Ann.* **41,** 228–230 (1959).
15. Immerzeel, W. W., Pellicciotti, F. & Bierkens, M. F. P. Rising river flows throughout the twenty-first century in two Himalayan glacierized watersheds. *Nat. Geosci.* **6,** 742–745 (2013).
16. Ragettli, S. *et al.* Unraveling the hydrology of a Himalayan catchment through integration of high resolution in situ data and remote sensing with an advanced simulation model. *Adv. Water Resour.* **78,** 94–111 (2015).
17. Linsbauer, A., Paul, F. & Haeberli, W. Modeling glacier thickness distribution and bed topography over entire mountain ranges with GlabTop: Application of a fast and robust approach. *J. Geophys. Res. Earth Surf.* **117,** 1–17 (2012).
18. Frey, H. *et al.* Estimating the volume of glaciers in the Himalayan & Karakoram region using different methods. *Cryosphere* **8,** 2313–2333 (2014).
19. Kääb, A., Berthier, E., Nuth, C., Gardelle, J. & Arnaud, Y. Contrasting patterns of early twenty-first-century glacier mass change in the Himalayas. *Nature* **488,** 495–498 (2012).

© 2017 Macmillan Publishers Limited, part of Springer Nature. All rights reserved.

20. Benn, D. I. & Lehmkuhl, F. Mass balance and equilibrium-line altitudes of glaciers in high-mountain environments. *Quat. Int.* **66,** 15–29 (2000).
21. Farinotti, D. *et al.* Substantial glacier mass loss in the Tien Shan over the past 50 years. *Nat. Geosci.* **8,** 716–722 (2015).
22. Gardner, A. S. *et al.* A reconciled estimate of glacier contributions to sea level rise: 2003 to 2009. *Science* **340,** 852–857 (2013).
23. Shea, J. M. & Immerzeel, W. W. An assessment of basin-scale glaciological and hydrological sensitivities in the Hindu Kush - Himalaya. *Ann. Glaciol.* **57,** 308–318 (2016).
24. Bliss, A., Hock, R. & Radić, V. Global response of glacier runoff to twenty-first century climate change. *J. Geophys. Res.* **119,** 1–14 (2014).
25. Mihalcea, C. *et al.* Spatial distribution of debris thickness and melting from remote-sensing and meteorological data, at debris-covered Baltoro glacier, Karakoram, Pakistan. *Ann. Glaciol.* **48,** 49–57 (2008).
26. Rounce, D. R., Quincey, D. J. & McKinney, D. C. Debris-covered glacier energy balance model for Imja-Lhotse Shar Glacier in the Everest region of Nepal. *Cryosphere* **9,** 2295–2310 (2015).
27. Rowan, A. V., Egholm, D. L., Quincey, D. J. & Glasser, N. F. Modelling the feedbacks between mass balance, ice flow and debris transport to predict the response to climate change of debris-covered glaciers in the Himalaya. *Earth Planet. Sci. Lett.* **430,** 427–438 (2015).

Supplementary Information is available in the online version of the paper.

Acknowledgements This project has received funding from the European Research Council (ERC) under the European Union's Horizon 2020 research and innovation programme (grant agreement number 676819), The Netherlands Organization for Scientific Research under the Innovational Research Incentives Scheme VIDI (grant agreement 016.181.308), from the Climate-KIC programme of the European Institute of Innovation & Technology (EIT), and from the UK Government's Department for International Development and the International Development Research Centre, Canada, through the Himalayan Adaptation, Water and Resilience (HI-AWARE) consortium. We thank E. Berthier and D. Scherler for supplying the validation data.

Author Contributions W.W.I., P.D.A.K. and M.F.P.B. designed the study; P.D.A.K. performed all analyses; A.F.L. contributed the climate change scenarios; P.D.A.K. and W.W.I. wrote the manuscript with suggestions from M.F.P.B. and A.F.L.

Author Information Reprints and permissions information is available at www.nature.com/reprints. The authors declare no competing financial interests. Readers are welcome to comment on the online version of the paper. Publisher's note: Springer Nature remains neutral with regard to jurisdictional claims in published maps and institutional affiliations. Correspondence and requests for materials should be addressed to P.D.A.K. (P.D.A.Kraaijenbrink@uu.nl).

Reviewer Information *Nature* thanks J. G. Cogley and D. Farinotti for their contribution to the peer review of this work.

© 2017 Macmillan Publishers Limited, part of Springer Nature. All rights reserved.

METHODS

Debris classification. The extent of debris cover on HMA glaciers was mapped for the entire area within the glacier outlines defined in the RGI5.0[8] for the RGI regions Central Asia, South Asia East and South Asia West. Debris-free ice was distinguished from debris-covered ice by using a normalized difference snow index[28] (NDSI). We calculated the NDSI from a Landsat 8 OLI composite that was produced by a pixel-wise selection of the scene with the highest brightness temperatures of thermal infrared (TIR) band 10 in the Landsat 8 top-of-atmosphere reflectance archive. The procedure, performed in Google Earth Engine[29], ensures a composite image that has: (1) no cloud cover, as clouds are colder than both snow and debris; (2) the smallest amount of shadow, as shadows are colder than sunlit terrain; and (3) the smallest amount of snow-covered debris, because debris is warmer than snow. Pixels were classified as debris for an NDSI below 0.25, a threshold determined by visual comparison of classification results with the imagery. A maximum slope constraint of 24° was set for debris cover[30] on 1 arcsec Shuttle Radar Topography Mission elevation data[31] (SRTM) to prevent misclassification of rock outcrops as debris, which set 23% of the pixels in the debris-covered class to debris-free.

Supraglacial ponds and lakes are often present on debris-covered tongues and are generally associated with the presence of ice cliffs. Recent findings have revealed that ponds and cliffs may accelerate local melt considerably[32], and are thus important to include in the analysis. Pond classification was performed by applying an upper threshold of −0.1 to the normalized difference vegetation index[33] (NDVI) for pixels classified as debris. A maximum slope of 20° and minimum brightness temperature of 10 °C were set as secondary constraints. Ponds misclassified as debris-free ice were identified by selecting connected groups of fifty or fewer debris-free pixels, and applying the same secondary constraints.

Classification accuracy was evaluated visually for a 1,000-pixel sample. A total of 800 samples were equally distributed over the classes debris-covered ice and debris-free ice in a stratified random sampling procedure. A 200-pixel sample was taken for the less abundant supraglacial lake class. The overall classification accuracy is 91% (Supplementary Table 2).

Ice thickness modelling. To obtain region-wide glacier thicknesses, we implemented the GlabTop2 model[18,34] using RGI glacier outlines and the SRTM data set (Supplementary Fig. 3). The model calculates ice thickness for each pixel within a glacier outline using a basal shear stress estimation and local slope. All calibrated input parameters of the model[18] were maintained, except the spatial density of random points for which the thickness is calculated in the GlabTop2 algorithm. This was reduced by a factor of 9 to account for the difference in spatial resolution of the elevation data sets used in the original study[18] (3 arcsec) and in this study (1 arcsec). This resulted in approximately the same number of random points per glacier in both cases. In addition, we have improved the computational efficiency of the model by calculating the local slope using a circular neighbourhood filter. The radius of this circular filter is a function of the glacier size, but constrained between 30 and 300 m. The minimum slope that is used in the thickness calculations was set to 2° to prevent unrealistically thick ice for the mountain glaciers of HMA.

Mass balance gradient and mass redistribution model. *Concept.* To model each glacier in the study area, we developed a mass balance gradient (MBG) model[20] in combination with a mass redistribution component. The model concept is illustrated in Supplementary Fig. 4. We constructed the MBG model, in which mass balance is expressed as a function of elevation, based on 6–25 equal elevation bands, depending on a glacier's area. Glaciers with an area of less than 0.4 km^2 were discarded from analysis, as a minimum number of pixels is required per elevation band to enable model simulations. In total, only 9.8% of the area and 0.7% of the volume were excluded from the analysis (Supplementary Table 1, Supplementary Fig. 1).

The annual ablation at the terminus (metres water equivalent per year) is calculated by

$$b_1 = \mathrm{DD} \times \mathrm{DDF}^{\mathrm{C}} \tag{1}$$

where DD is the mean annual positive degree–day sum obtained from the WATCH-Forcing-Data-ERA-Interim data set[35] (WFDEI) over the period 1996–2014, downscaled using SRTM and a temperature lapse rate of 0.0065 °C m^{-1}. $\mathrm{DDF}^{\mathrm{C}}$ is the degree–day factor for debris-free (clean) ice[36]. Mass balance for the remaining elevation bands is determined by applying a linear MBG with respect to elevation:

$$b_i = b_1 + (z_i - z_1)\frac{\mathrm{d}b}{\mathrm{d}z} \tag{2}$$

where z_i is the surface elevation of elevation band i.

The annual maximum accumulation is constrained by the mean annual precipitation at each glacier ($b_{\max} = P$). Here the ERA-Interim reanalysis data[37] for the period 1996–2015 was used, as high-elevation precipitation is represented better in ERA-Interim than in other large-scale reanalysis products[36,38,39].

Debris on glaciers is generally thin at higher elevations and thickens towards the terminus. To incorporate a spatially variable melt reduction that corresponds to these different debris thicknesses[14], we applied a simplified surface temperature inversion method[25,40,41]. Surface temperatures were derived from TIR band 10 of the Landsat 8 composite by correcting for emissivity using the ASTER global emissivity product. For the debris-covered area of a glacier, we assumed that the lowest surface temperature corresponds to a debris thickness of 1 cm, and that the 95th percentile corresponds to thick debris[26,41–43] (Supplementary Table 4). Following from the nonlinear relation between thickness and temperature reported in literature[25,40,41], we estimated debris thickness using exponential scaling:

$$h = \mathrm{e}^{\frac{(T - T_{\min})\ln h_{\max}}{T_{\mathrm{P95}} - T_{\min}}} \tag{3}$$

where h is debris thickness in cm, T is the surface temperature, $T_{\min}$ is the minimum surface temperature of the debris, $h_{\max}$ is the thickness that corresponds to the 95th percentile surface temperature, and T_{P95} is the 95th percentile surface temperature. A map of melt reduction was subsequently produced using a relative relation between debris thickness and ablation, which was constructed using data from the literature[14,43–47] (Supplementary Fig. 5). To account for the high melt observed for surface features on debris-covered glaciers we have attributed a melt enhancement factor to supraglacial ponds that is ten times as high as the melt of thick debris, based on detailed research on a debris-covered glacier in the Himalaya[32].

For each elevation band, we calculate an effective degree–day factor DDF_i from the fractional class coverages of each band and their respective melt factors. This is used to calculate a corrected negative mass balance using:

$$b_i^{\mathrm{Corrected}} = b_i - b_i\left(1 - \frac{\mathrm{DDF}_i}{\mathrm{DDF}^{\mathrm{C}}}\right) \tag{4}$$

Given a terminus ablation defined by the degree–day sum, maximum accumulation defined by precipitation and the mass-balance debris correction (equation (4)), the slope of the mass balance gradient db/dz (metres water equivalent per year per metre) is determined by minimization (Supplementary Fig. 4) of:

$$\left(\sum_{i=1}^{n}(b_i a_i) - B_{\mathrm{obs}}\right)^2 \tag{5}$$

with B_{obs} being the observed glacier mass balance, which is discussed in the next section, and a_i the surface area of elevation band i.

The determination of $\mathrm{d}b/\mathrm{d}z$ by minimization of equation (5) resulted occasionally in unrealistically low ELAs, especially for large glaciers in low-precipitation regions. This is largely due to an underestimation of the high-altitude precipitation for such glaciers, which is a known issue of the gridded climate products[36]. To correct for this issue, we increased the maximum accumulation of a glacier iteratively (up to a maximum of 3,000 mm) until the modelled ELA was at least greater than the 25th percentile of its SRTM elevation.

Regional observed mass balance. Data on recent glacier mass balances in HMA are relatively sparse. To obtain a region-covering data set we have therefore compiled recent regional mean mass balances and inter-glacier mass balance variability from multiple remote sensing and *in situ* studies[5,21,22,48–52] (Supplementary Table 3). The regional mass balance data were converted to a grid of points at an equidistance of approximately 1°, covering only the regions for which data were available. Kriging interpolation of the points was performed subsequently to obtain coverage for the entire HMA. The final regional data were acquired by aggregating the interpolated product. A comparison with regional mass balance data sets that are less complete[50,53] (Supplementary Fig. 15) shows there is overall agreement, but also that there are some clear differences. This indicates that there is still a need for a more consistent and comprehensive mass balance data set for the entire HMA.

Future climate implementation. To simulate future changes, we shifted the calibrated present-day mass balance curve using the temperature sensitivity of the ELA[23], which can range from about 55 to 200 m °C^{-1} depending on local climate, and a projected temperature trajectory between the present and the EOC (Supplementary Fig. 8). The maximum accumulation of a glacier was changed according to projected changes in precipitation for the same period (Supplementary Fig. 9). The ensemble of temperature and precipitation projections that was used was compiled from all GCMs for all representative concentration pathways (RCPs) within the CMIP5 multi-model ensemble[7] ($n = 110$, Supplementary Table 5). From the ensemble, we have selected models for the 1.5 °C scenario that have a global temperature change between pre-industrial (1851–1880) and the EOC (2071–2100) of 1.4–1.6 °C ($n = 6$).

© 2017 Macmillan Publishers Limited, part of Springer Nature. All rights reserved.

For the GCM runs, we extracted grids of the projected changes in average air temperature and precipitation between present (1996–2015) and multiple future time slices of five years (2006–2010, 2011–2015, …, 2096–2100). The GCM grids of varying spatial resolution were all interpolated to 0.05° resolution. The changes for temperature and precipitation were superimposed on the reference climatology, that is, mean WFDEI temperature (1996–2014) and mean ERA-Interim precipitation (1996–2015), to generate the relative changes with respect to the present day. To obtain the final forcing input for the MBG model, a moving window average was determined for each of the 5-year slices to obtain moving 30-year climatological changes, which were subsequently interpolated to a yearly time series.

Dynamic mass redistribution. Ice mass redistribution within individual glaciers was performed using a lumped parameterization of ice flow[54] to each elevation band *i*:

$$Q_i = \chi a_i H_i^5 \nabla z_i^3 \quad (6)$$

where Q_i is the volume that flows to the elevation band below, a_i the surface area, H_i the mean ice thickness, and ∇z_i the gradient of the glacier surface at elevation band *i*. Parameter χ describes ice rheology and governs the flow rate. It was determined separately for each glacier at the first time step by optimization of the unknown ∇z_i. This can be performed by constraining the optimization by (1) the glacier length defined in the RGI database, (2) a stagnant glacier terminus ($Q_1 = 0$), (3) the observed mass balance and (4) the degree–day sum and precipitation. Using this procedure, an optimal combination of the unknown ∇z_i and χ is found that satisfies the glacier hypsometry, mass balance and the external forcing. Based on mass balance b_i of an elevation band that follows from the mass balance curve, and the computed ice flux, the ice thickness is updated each time step for each elevation band.

The model runs were performed transiently for the period 2005–2100 with a yearly time step. At each time step b_i was updated according to the translated mass balance curve and mass was redistributed. After calculating new volumes for each elevation band, a_i was updated using the exact volume–area relation for each band *i*, which was determined separately for each band from the modelled glacier bed shape, that is, the ice thickness, by fitting a predictive spline model at the first time step. Cross-sections and maps that show examples of modelled ice thickness over time are presented in Supplementary Figs 7 and 11, respectively. In addition, animations of modelled ice thickness are available as Supplementary Videos for a selection of glaciers.

Glaciers can have elevation bands that have much lower volumes than the rest of the glacier, for example, at ice falls. Consequently, the ice flux through these bands can be a multiple of the ice volume present in the band itself, which cannot be resolved properly within the model time step and results in numerical instability. To counteract this, we have constrained the net flux of an elevation band to 20% of its initial ice volume; however, mass is conserved by iteratively transferring excess to adjacent lower elevation bands. The value of 20% is the largest threshold that resulted in numerically stable simulation.

The model concept does not allow ice to advance beyond the initial glacier extent. To account for glacier advance, all excess ice volume is captured in the lowest elevation band. Surface area and ablation rate for the band are adapted proportionally to the excess volume. In absence of any knowledge about the bed shape of lower elevation bands, we have chosen to calculate the increase in area caused by excess mass using a linear relation between the volume and area of a glacier. The extent to which an advance reaches lower elevation bands that are outside the glacier's initial extent is governed by the ratio between the advancing volume and the mean volume of all elevation bands, that is, the advance reaches exactly one elevation band lower if the volumes are equal. Finally, the ablation of the lowest elevation band is scaled using the mass balance gradient to incorporate the advance.

Uncertainty. To express the uncertainty in the model parameters, we applied a Monte Carlo approach to the MBG model (Supplementary Fig. 6) in which we sampled five different model input variables: (1) degree–day sum, (2) maximum precipitation, (3) degree–day factor for debris-free ice, (4) debris thickness and (5) observed regional mass balance. Sampling means, standard deviations, ranges and distributions are presented in Supplementary Table 4. Following deterministic runs for each climate model projection that use the mean parameter values as input, we drew ten random combinations of input parameters for each of the 110 climate model projections of each modelled glacier. This yielded a total of 1,210 different model realizations per glacier.

Model validation. The accuracy of the model dynamics was evaluated using two independent data sets. We first used a geodetic data set of elevation changes[50] (dH) for the period 1999–2011 to compare observed and modelled dH of the ablation zone for eight separate regions. The model was forced with current climate conditions and run for ten years. Regional mass balances for the validation run were taken from the validation data set itself (Supplementary Fig. 15) to enable optimal evaluation of the model dynamics. There is generally good agreement between modelled and observed dH on a regional level (Supplementary Fig. 16a), for both debris-free and debris-covered glaciers. Apart from compensating effects that can never be ruled out if individual processes are not monitored separately at individual glaciers, this indicates that accumulation, ablation, debris effect, and mass redistribution are well represented in the model at the regional scale. There is, however, large variability within the regions (Supplementary Fig. 16a), and at the glacier scale there can be differences between observed and modelled dH. This is inevitable, however, since the large differences in glacier-specific boundary conditions caused by complex local topography and climate are impossible to model with the data that are currently available. For interpretation of the model results, regional aggregation is therefore important.

For a second validation of the model dynamics, a data set of satellite-derived frontal changes of 255 glaciers[55] distributed over six regions in the HMA was compared with the model results. The model, being based on a lumped approach, cannot provide frontal changes directly. We have therefore estimated the changes in the terminus position by linear scaling of the length of the lowermost elevation band (or multiple bands in the case of disappearance of the lowermost band) by its relative volume loss. Again, a ten-year model run forced by current climate conditions was used, but now with the original mass balances (Supplementary Table 3). Supplementary Fig. 17a shows that the observed and modelled frontal changes are generally in agreement. There is disagreement for the Karakoram and West Kun Lun, which is likely to be caused by the abundance of surging glaciers in the Karakoram, a process not incorporated in the model, and the very minimal mass balance forcing used for the entire West Kun Lun.

To determine whether the glaciers' ablation and accumulation are well represented in the MBG model procedure, we have also compared the ELAs that follow from the MBG fit with reported regional ELA[50] and snowline elevation[55] estimates. For both data sets, the modelled ELAs agree well (Supplementary Figs 16b, 17b), indicating that boundary conditions and model processes that are part of the MBG fit, for example, degree–days, precipitation and debris melt reduction, are of the correct magnitude.

Code availability. The Google Earth Engine classification code (JavaScript) and the model code (R) are available at http://github.com/kraaijenbrink/nature-2017.

Data availability. Supplementary data can be downloaded from http://www.mountainhydrology.org/data-nature-2017. This includes grids per glacier of the debris classification and ice thickness, model forcing data, and region-aggregated data in vector format. Other relevant data are available from the authors upon request.

28. Hall, D. K., Riggs, G. A. & Salomonson, V. V. Development of methods for mapping global snow cover using moderate resolution imaging spectroradiometer data. *Remote Sens. Environ.* **54,** 127–140 (1995).
29. Google Earth Engine Team. *Google Earth Engine: A Planetary-Scale Geo-Spatial Analysis Platform* (2017).
30. Paul, F., Huggel, C. & Kääb, A. Combining satellite multispectral image data and a digital elevation model for mapping debris-covered glaciers. *Remote Sens. Environ.* **89,** 510–518 (2004).
31. Farr, T. *et al.* The shuttle radar topography mission. *Rev. Geophys.* **45,** RG2004 (2007).
32. Immerzeel, W. W. *et al.* High-resolution monitoring of Himalayan glacier dynamics using unmanned aerial vehicles. *Remote Sens. Environ.* **150,** 93–103 (2014).
33. Lillesand, T., Kiefer, R. W & Chipman, J. *Remote Sensing and Image Interpretation* 7th Edn (John Wiley & Sons, 2015).
34. Farinotti, D. *et al.* How accurate are estimates of glacier ice thickness? Results from ITMIX, the Ice Thickness Models Intercomparison eXperiment. *Cryosphere* **11,** 949–970 (2017).
35. Weedon, G. P. *et al.* Data methodology applied to ERA-Interim reanalysis data. *Wat. Resour. Res.* **50,** 7505–7514 (2014).
36. Immerzeel, W. W., Wanders, N., Lutz, A. F., Shea, J. M. & Bierkens, M. F. P. Reconciling high-altitude precipitation in the upper Indus basin with glacier mass balances and runoff. *Hydrol. Earth Syst. Sci.* **19,** 4673–4687 (2015).
37. Dee, D. P. *et al.* The ERA-Interim reanalysis: configuration and performance of the data assimilation system. *Q. J. R. Meteorol. Soc.* **137,** 553–597 (2011).
38. Palazzi, E., Von Hardenberg, J. & Provenzale, A. Precipitation in the Hindu-Kush Karakoram Himalaya: observations and future scenarios. *J. Geophys. Res. Atmos.* **118,** 85–100 (2013).
39. Dahri, Z. H. *et al.* An appraisal of precipitation distribution in the high-altitude catchments of the Indus basin. *Sci. Total Environ.* **548–549,** 289–306 (2016).
40. Foster, L. A., Brock, B. W., Cutler, M. E. J. & Diotri, F. A physically based method for estimating supraglacial debris thickness from thermal band remote-sensing data. *J. Glaciol.* **58,** 677–691 (2012).
41. Rounce, D. R. & McKinney, D. C. Debris thickness of glaciers in the Everest Area (Nepal Himalaya) derived from satellite imagery using a nonlinear energy balance model. *Cryosphere* **8,** 1317–1329 (2014).
42. Nicholson, L. & Benn, D. I. Properties of natural supraglacial debris in relation to modelling sub-debris ice ablation. *Earth Surf. Process. Landf.* **38,** 490–501 (2013).

© 2017 Macmillan Publishers Limited, part of Springer Nature. All rights reserved.

43. Juen, M., Mayer, C., Lambrecht, A., Han, H. & Liu, S. Impact of varying debris cover thickness on ablation: a case study for Koxkar Glacier in the Tien Shan. *Cryosphere* **8,** 377–386 (2014).
44. Mihalcea, C. *et al.* Ice ablation and meteorological conditions on the debris-covered area of Baltoro glacier, Karakoram, Pakistan. *Ann. Glaciol.* **43,** 292–300 (2006).
45. Kayastha, R. B., Takeuchi, Y., Nakawo, M. & Ageta, Y. Practical prediction of ice melting beneath various thickness of debris cover on Khumbu Glacier, Nepal, using a positive degree-day factor. *IAHS-AISH Publication* **264,** 71–81 (2000).
46. Nicholson, L. I. & Benn, D. I. Calculating ice melt beneath a debris layer using meteorological data. *J. Glaciol.* **52,** 463–470 (2006).
47. Collier, E. & Immerzeel, W. W. High-resolution modeling of atmospheric dynamics in the Nepalese Himalaya. *J. Geophys. Res. Atmos.* **120,** 9882–9896 (2015).
48. Zhang, Z. *et al.* Mass change of glaciers in Muztag Ata – Kongur Tagh, Eastern Pamir, China from 1971/76 to 2013/14 as derived from remote sensing data. *PLoS One* **11,** e0147327 (2016).
49. Yao, T. *et al.* Different glacier status with atmospheric circulations in Tibetan Plateau and surroundings. *Nat. Clim. Chang.* **2,** 663–667 (2012).
50. Gardelle, J., Berthier, E., Arnaud, Y. & Kääb, A. Region-wide glacier mass balances over the Pamir-Karakoram-Himalaya during 1999–2011. *Cryosphere* **7,** 1263–1286 (2013).
51. Ke, L., Ding, X. & Song, C. Heterogeneous changes of glaciers over the western Kunlun Mountains based on ICESat and Landsat-8 derived glacier inventory. *Remote Sens. Environ.* **168,** 13–23 (2015).
52. Sorg, A., Bolch, T., Stoffel, M., Solomina, O. & Beniston, M. Climate change impacts on glaciers and runoff in Tien Shan (Central Asia). *Nat. Clim. Chang.* **2,** 725–731 (2012).
53. Cogley, J. G. Geodetic and direct mass-balance measurements: comparison and joint analysis. *Ann. Glaciol.* **50,** 96–100 (2009).
54. Marshall, S. J. *et al.* Glacier water resources on the eastern slopes of the Canadian Rocky Mountains. *Can. Water Resour. J.* **36,** 109–134 (2011).
55. Scherler, D., Bookhagen, B. & Strecker, M. R. Spatially variable response of Himalayan glaciers to climate change affected by debris cover. *Nat. Geosci.* **4,** 156–159 (2011).

© 2017 Macmillan Publishers Limited, part of Springer Nature. All rights reserved.